ICAS 2020 SHANGHAI
International Council of the Aeronautical Sciences
32nd Congress of the International Council of the Aeronautical Sciences
September 6-10, 2021
Pudong Shangri-La, Shanghai, China

PROPELLER WAKE - OBJECT INTERACTION USING A FREE WAKE MODEL UTILIZING LOCAL MESH SEPARATION

Moritz Thiele, Dimitrios Salassidis & Mirko Hornung

Institute of Aircraft Design, Technical University of Munich, Germany

Abstract

Interactions between UAV propellers and other objects are investigated with respect to their mutual influences using a Vortex Lattice Model for all considered bodies, which are coupled with a Free Wake Model. To increase overall calculation performance the mirror method commonly used for the prediction of helicopter ground effects is modified and applied to the obstacles. The wake vortex sheets are furthermore able to separate and subsequently flow around an obstacle. Wake vortices are possibly reunited after obstacle passage. This procedure greatly enhances the computational accuracy and enables the consideration of more complex obstacles. The model is embedded in the "Synthesis and Analysis Rotor Environment" (SARF) data framework which provides a flexible and dynamic simulation environment that reduces manual work on the creation of the geometric mesh.

Keywords: Vortex-Lattice Method, Propeller Wake, Vortex Separation, Vortex Interaction

1. Introduction

The increasing use of civil and military electrical Vertical Takeoff and Landing (eVTOL) Unmanned Aerial Vehicles (UAV) requires highly safe, reliable and efficient UAV configurations. A meaningful and efficient integration of the rotors is a key task of UAV design for all propulsive concepts. The mutual influence between a rotor and other objects in its vicinity is thereby of particular interest as a significant disturbance of the rotor intake or wake will generate noise and lead to performance losses. The goal of this paper is to model and predict the wake geometry of a propeller in an arbitrary flow state (hover, cruise, inclined flow) and to determine the impact of its interaction with other objects in its vicinity. This model is intended to be used in the preliminary UAV design process to assess multiple early configurational UAV variants and assist in the evaluation of design trade-off studies. Its primary goal is to enable a UAV design engineer to quickly assess the impacts of the propeller position on a UAV, e.g. a tractor or pusher configuration. Therefore, it is not suitable to tackle this problem using sophisticated CFD calculations but rather using methods, which are faster, provide more flexibility and enable the consideration of multiple alternative configurations without the need for any manual meshing activity.

With this model, UAV design trade-offs concerning the propeller efficiency can be conducted, which will lead to a more optimized UAV powertrain in an earlier design stage. The effect of the wake obstruction can be assessed by comparing the bound vortex strength on the blades of a clean with an obstructed configuration.

Models solely predicting the wake geometry of a propeller are abundant. One of the first empirical models that could distinguish between the wake vortex sheets shed at the trailing edge of the blade and the tip vortex was developed by Landgrebe [1]. More advanced models have since been established to predict the geometry of an unobstructed propeller wake e.g. by Giovanetti [2] or Panayotov [3]. However these models fail to resolve individual wake vortices that can be used to determine the wake's influence on other bodies. Considering obstacles in the wake is therefore not possible with these models.

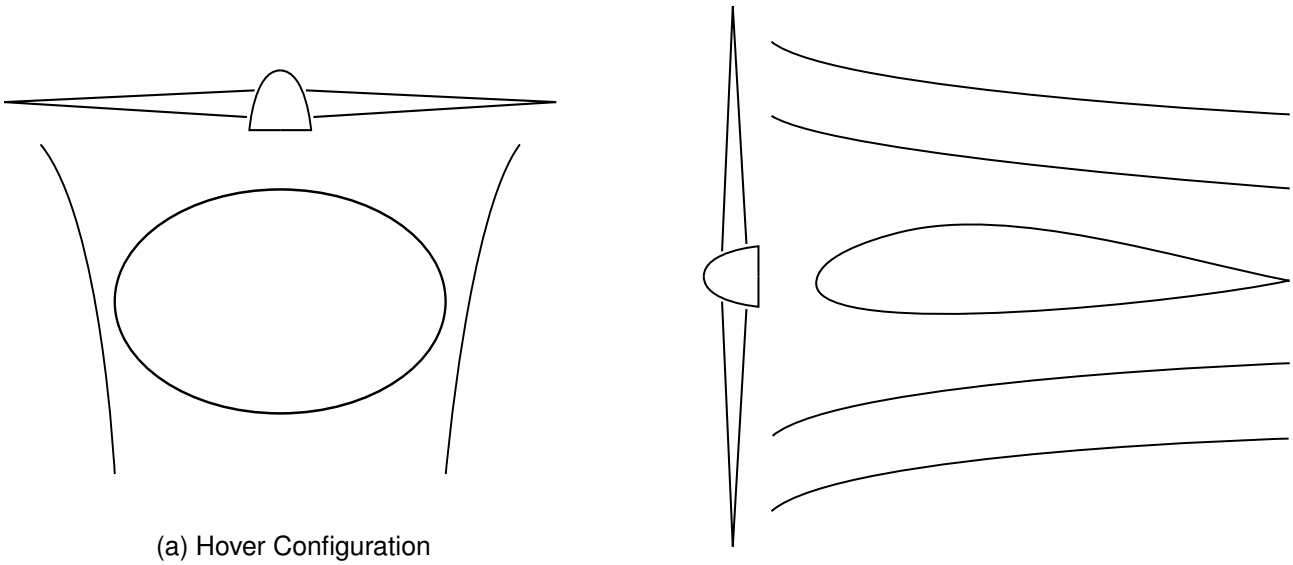

(a) Hover Configuration

(b) Cruise Configuration

Figure 1 – Propeller - Obstacle Configuration Options

The analysis of the interaction between a propeller wake and an object such as a wing or a fuselage without CFD but with faster methods has also been in the focus of many publications. Much work has already been published for classical propeller-wing-tractor configurations as shown schematically in Fig. 1b. However, the recent rise of eVTOL UAV has sparked a special interest on the configuration of a hover propeller above an arm of a multicopter or above the UAV fuselage as shown in Fig. 1a.
Especially publications focusing on the former layout Fig. 1b mostly cared about the impact of the propeller on the wing performance. Veldhuis [4] used an advanced actuator disc model for assessing the propeller while choosing a VLM model for the wing. Marretta [5] took a similar approach. The near wake of a propeller was modeled by vortex filaments traveling downstream influenced by a contraction factor and an axial convection velocity. The far wake was modeled by an infinite solenoid having constant diameter. This approach was used to impose an additional flow component on the affected wing areas.
Previous work considering the configuration Fig. 1a, mostly cared about the propeller rather than the wing performance which is why they in general chose a more sophisticated model for the assessment of the propeller. The model developed by Abedi [6] provides the baseline model as described in the first part of this publication. This model, however, lacks the consideration of obstacles. Cao [7] focused on the interaction effects of a rotor with a fuselage and used a similar model to describe the rotor geometry. The wake resolution is only limited to few time steps and is then reduced to a simple tip vortex filament for the far wake.
The model presented in this paper aims to describe the wake vortex elements explicitly into the far wake region in order to capture all interference effects of a propeller and an obstacle geometry. The basic VLM theory is therefore implemented within the "Synthesis and Analysis Rotor Environment" (SARF) data framework which was first developed in [8] and further refined in [9]. The discretization is based on the geometry stored in the framework and will be automatically created. Explicit steps have been undertaken to enhance the transient behavior of the wake vortex sheets by considering effects like vortex separation by obstacles within the baseline model.

2. Technical Approach

A Vortex Lattice Model (VLM) was chosen for both the propeller and an obstacle in the wake as the focus of this work lies on the impact of other objects on the propeller performance. The area between the objects is modeled with a Free Wake Model (FWM) that is coupled with the VLM code rather than a fixed helical structure. This enables an individual resolution of wake vortex rings which can roam the wake area freely. As a result, an obstacle can be placed at an arbitrary position of the computational area. Each time step is resolved individually and explicitly, which enables a depiction of transient

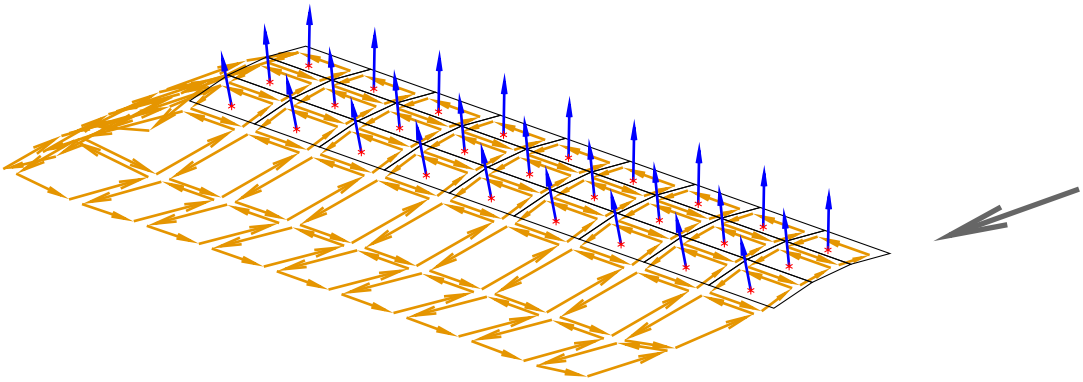

Figure 2 – VLM Model for cambered blade

behavior and allows relative and dynamic movement between the propeller and the obstacle. The global transient inflow can be superimposed on the induced velocities and can be considered from an arbitrary direction. Several changes to the standard VLM model have been implemented and are described in detail in the following chapters. Obstacle surfaces are treated by the mirror method that is common when assessing the ground effect. Furthermore, the wake sheets are able to be separated by an obstacle where the wake-sheet will flow around the obstacle body rather than through it. The results show a positive effect on the overall computational stability and simulation accuracy.

2.1 VLM Model Theory

The basic VLM model is based on a classical lifting surface theory of vortex ring elements according to Katz [10, p. 340] that is also applied by Abedi [6]. It is based on the incompressible potential theory that is derived from the Laplace equation using Green's Identity. The boundary condition that has to be fulfilled is the zero normal flow across all lifting surfaces. The potential flow field around a body is modeled by dipoles because no thickness effects - which would require the modeling of sources - are considered due to the geometry being represented as a thin lifting surface. A dipole panel of constant vortex strength corresponds to a closed vortex loop with the circulation strength Γ. The main assumptions in the model in accordance with [10] and [11] are:

- The flow field is friction-less, rotation-free and incompressible
- The bound circulation strength Γ is defined according to the Kutta-Condition thus asserting, that the vorticity present at the trailing edge (TE) of a lifting body will be shed in the wake smoothly [12].
- A vortex will form a closed vortex ring of constant vorticity following the second Helmholtz Vortex Theorem once it has been shed into the wake.

A lifting surface such as a propeller blade shown in Fig. 2 is discretized along its camber line and along its span into multiple sections each. The thickness of the lifting surface is disregarded, which prevents the calculation of a local pressure distribution. This discretization is used to create a paneled camber sheet drawn in black along the geometry. This model also allows for a variable pitch and chordlength along the span of a blade which is especially important when assessing highly twisted UAV propellers. Each panel defines a vortex ring (orange) and corresponding normal vector $\vec{n}$ (blue) whose origin is at the collocation point. The collocation point that is indicated by a red star is located at the 75% point of each panel and the center of a vortex ring which implies the vortex rings being shifted from the panels by a quarter of their length in the direction of the TE. The individual vortices starting and ending at the corner points CP_i of the vortex ring shown in orange are of constant vorticity Γ. A detailed view of one vortex ring and the normal vector is presented in Fig. 3. Note the normal vector $\vec{n}$ being perpendicular to each bound vortex ring, not the corresponding geometric panel. These individual vortex filaments are considered when assessing the vortex influence on other points in the design space which will be explained in depth below.

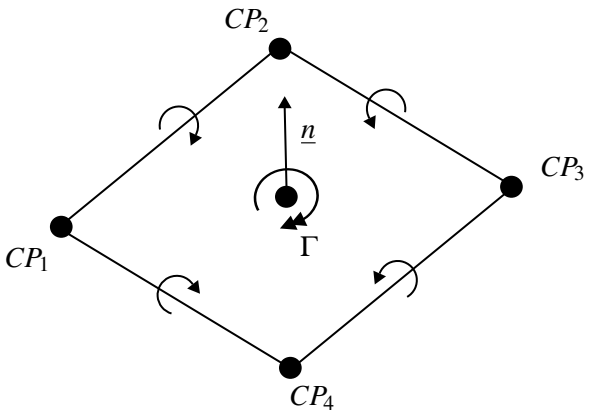

Figure 3 – Schematic of a single vortex ring

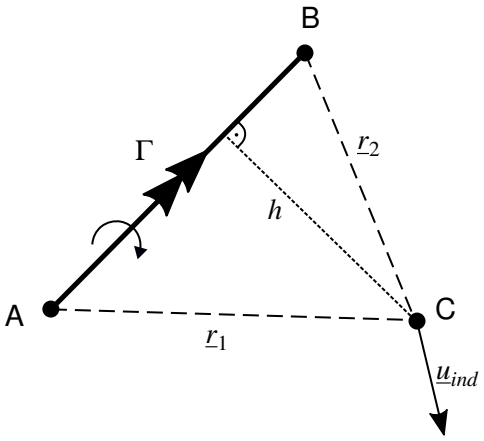

Figure 4 – Induced Velocity from a single vortex filament according to Biot-Savart-Law

The bound vortex panels shown in Fig. 2, that are located on the blade are shed into the wake at the TE with a vortex strength that is constant over the shedding motion according to the Kutta condition. This means, that every new wake vortex carries the circulation strength of the vortex ring associated with the blade panel at the TE of the rotor blade. Furthermore, according to the Kelvin theorem this vortex strength in the free wake is constant for all future time steps:

$$\frac{d\Gamma}{dt} = 0 \tag{1}$$

Two rows of wake vortex rings are shown in Fig. 2 which have been generated by calculating two time steps where one row has been shed for each time step. Each shedding motion is achieved by having the vortex corner points CP_i corresponding to the TE fixed in place (which are actually already located behind the blade due to the displaced vortex ring relative to the geometric panel) while the blade moves forward for one time step. These points will then form a new wake vortex ring with the two corner points at the new position of the blade TE. The corner points of all wake vortex rings will subsequently move freely, influenced only by the overall inflow shown by the gray arrow in Fig. 2 and the mutually induced velocities. The left border of the blade shows the rotor tip which exhibits tip losses. Those losses are modeled by the tip panels also shedding vortex rings in radial direction. The roll-up of these individual tip vortices to an effective tip vortex can be observed in the two wake panels following the blade tip. There are no losses on the right hand side of the geometry as hub losses are not considered although they could be modeled analogous to the tip losses. Losses in the hub area of UAV propellers are relatively small compared to classical helicopter blades and are thus not modeled here.

The mutually induced velocity by the individual vortex segments is calculated using the Biot-Savart Law. The analytical equation is quite straight forward, is given in Eq. (2) and visualized in Fig. 4. A vortex segment with the vorticity Γ will induce the velocity $\vec{u}_{ind}$ on an arbitrary point with a distance $\vec{h}$ from the vortex segment [13]

$$\vec{u}_{ind} = \int_S \frac{\Gamma}{4\pi} \frac{d\vec{l} \times \vec{h}}{\left|\vec{h}\right|^3}. \tag{2}$$

This equation holds for a continuous vortex and has to be discretized to be used with the vortex filaments presented above. The integral can be solved by Eq. (3) for a straight vortex filament between Points A and B inducing the velocity $\vec{u}_{ind}$ on the point C with the distances $\vec{r}_1 = \overrightarrow{AC}$ and $\vec{r}_2 = \overrightarrow{BC}$ between the respective points [6].

$$\vec{u}_{ind} = \frac{\Gamma}{4\pi} \frac{(|\vec{r}_1| + |\vec{r}_2|)(\vec{r}_1 \times \vec{r}_2)}{(|\vec{r}_1||\vec{r}_2|)(|\vec{r}_1||\vec{r}_2| + \vec{r}_1 \cdot \vec{r}_2)}. \tag{3}$$

Eq. (3) results in a singularity for $h \to 0$ which is why it must be desingularized using a factor K_V [14] that is defined by a model proposed by Vatistas [15]:

$$K_V = \frac{h^2}{\left(r_c^{2n} + h^{2n}\right)^{\frac{1}{n}}} \tag{4}$$

Bagai [16] suggests using $n = 2$ to deliver the most stable desingularization model which is also chosen in this work. The desingularized equation therefore yields:

$$\vec{u}_{ind} = K_V \frac{\Gamma}{4\pi} \frac{\left(|\vec{r}_1| + |\vec{r}_2|\right)\left(\vec{r}_1 \times \vec{r}_2\right)}{\left(|\vec{r}_1|\,|\vec{r}_2|\right)\left(|\vec{r}_1|\,|\vec{r}_2| + \vec{r}_1 \cdot \vec{r}_2\right)}. \tag{5}$$

Eq. (5) models the induced velocity to resemble rigid body rotation for $h < r_c$ and a potential vortex for $h > r_c$ with r_c being the core radius of the vortex. Defining the core radius r_c is more complex. In general there are two models to be found in literature:

- Setting r_c constant over the vortex age as it is used in [6].
- Bhagwat [14] proposed a dissipative viscous core model that leads to r_c expanding with advancing vortex age similar to the vortex model developed by Lamb [17].

The VLM model used in this paper uses the first approach, however the effects of a diffusive core model should also be assessed in future work. Eq. (5) can be separated in two parts which enables the separate evaluation of the geometric influence $a_{i,j}$ of a vortex filament j on a point i and the vorticity Γ_j:

$$a_{i,j}\,\Gamma_j = \vec{u}_{ind_i} \tag{6}$$

Each vortex will influence each bound collocation point and every wake corner point, thus the mutual interferences can be written as the following linear equation system as proposed by [10]:

$$AIC \times \Gamma = \begin{pmatrix} a_{1,1} & a_{1,1} & \cdots & a_{1,n} \\ a_{2,1} & a_{2,1} & \cdots & a_{2,n} \\ \vdots & \vdots & \ddots & \vdots \\ a_{m,1} & a_{m,1} & \cdots & a_{m,n} \end{pmatrix} \begin{pmatrix} \Gamma_1 \\ \Gamma_2 \\ \vdots \\ \Gamma_n \end{pmatrix} = \begin{pmatrix} \vec{u}_{ind_1} \\ \vec{u}_{ind_2} \\ \vdots \\ \vec{u}_{ind_m} \end{pmatrix} = \vec{U}_{ind} \tag{7}$$

The size of this matrix AIC is $(m \times n)$ with n vortices influencing m points of interest. Eq. (7) can be used for two aspects of the algorithm: Firstly, the calculation of induced velocities on wake elements where Γ is known. Secondly, Γ can also be determined on the bound vortex rings because the velocities present at the collocation points are known due to the boundary conditions and the existing wake structure.
The latter requires the calculation of the right hand side of Eq. (7) as it is described e.g. in [6]. This side of the equation is determined by evaluating the no-penetration boundary condition of the surface which requires the sum of all velocities in normal direction of the bound vortex rings at the collocation points (cp) being counteracted by $\vec{u}_{ind,i}$, which represents each element's induced velocity. This yields equation Eq. (8) for the induced velocity on the bound vortex rings (bvr) with index i:

$$\vec{u}_{ind,i} = RHS_i = -\left(\vec{u}_\infty + \Omega\vec{r} + \vec{u}_{ind,wake}\right)_i \cdot \vec{n}_{colp,i} \tag{8}$$

The right hand side (RHS_i) is composed of the inflow velocity, the rotational velocity and the velocity induced by all wake vortices.

Basic VLM Algorithm The basics presented in the previous section deliver all information needed to set up the basic VLM algorithm.
Initially, the propeller has to be discretized to fit the model as described above. One important assumption that is taken in this work is, that the propeller and all other obstacle geometries are stiff which implies, that the relative position of all it's collocation points stays constant for every time step. This enables the calculation of the corresponding AIC-Matrix containing the geometric influence coefficients used in Eq. (7) beforehand. The coefficients will stay constant in a body-fixed coordinate system that follows the propeller's rigid body rotation and movement. This reduces computational effort and enables a finer discretization of the blades. Similarly, the influence of the obstacle's bound vortices on the bound vortices of the propeller blades and vice versa are not considered in Eq. (8) as these structures are generally quite far apart. This saves additional computational effort as the two objects in general exhibit relative motion which makes it impossible to pre-compute the geometric influence matrix.

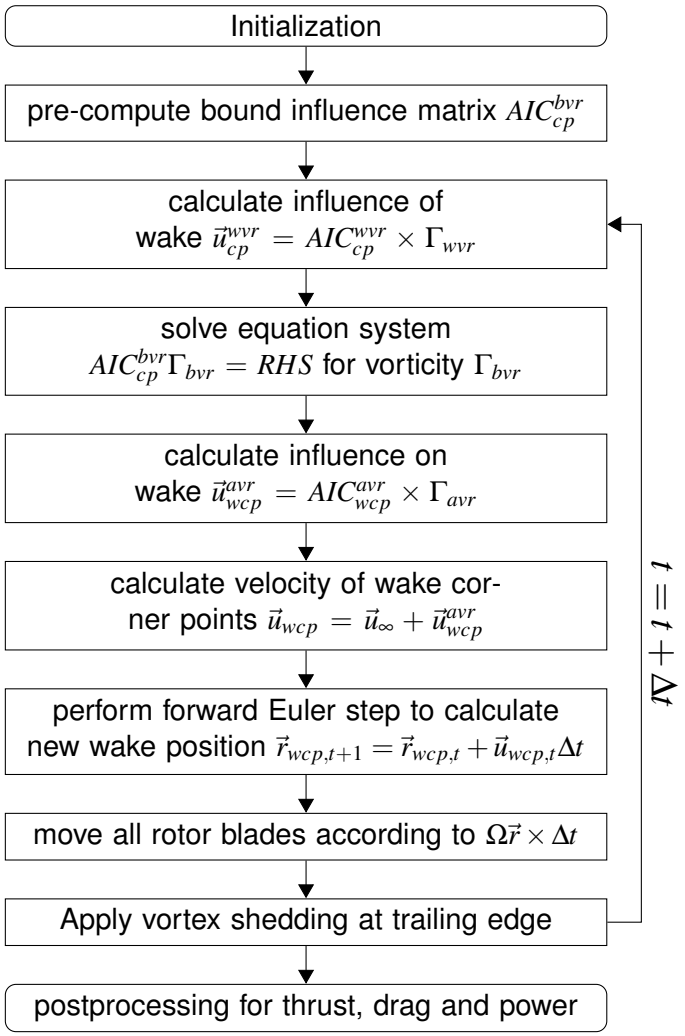

Figure 5 – VLM Algorithm Flowchart

Fig. 5 shows the basic flow chart of this time-marching algorithm. This flow chart only considers one propeller while the incorporation of the obstacles will be described below.
Induced velocities and AIC influence matrices are noted in the following manner with the abbreviated elements in the sub- and superscripts:

$$AIC_i^j \begin{cases} \text{superscript: influencing element} \\ \text{subscript: influenced element.} \end{cases} \qquad \text{with } i,j \in \begin{cases} \text{colocation points} & colp \\ \text{body vortex rings} & bvr \\ \text{wake vortex rings} & wvr \\ \text{wake corner points} & wcp \\ \text{all vortex rings} & avr \end{cases}$$

As a first step, the influence of all vortices in the wake on each bound vortex has to be determined. This is performed with Eq. (7). The vortex strength Γ is taken from the previous time step. The values for Γ_{bvr} are determined next by solving the linear equation system of Eq. (7) for Γ_{bvr}. This is then used to determine the influence of all present vortex rings on the wake corner points which is added to the global inflow velocity and subsequently used to perform an explicit Euler time step. The propeller blades and all bound elements are then rotated by one time step while vortex-shedding is used to generate a new row of wake vortex rings in the wake.
These steps are repeated for every time step or until convergence is achieved. Propeller characteristics can be calculated from the final vortex strength of the bound vortices. The lift produced by each bound vortex panel at a certain radial position y_j with a certain length in radial direction $\Delta\vec{y}_j$ is

calculated according to [10] by the following equation:

$$\vec{L}_{i,j} = \rho\, \vec{u}_{tot,i,j} \times \left(\Gamma_{i,j} - \Gamma_{i-1,j}\right) \Delta\vec{y}_{i,j} \qquad \text{for} \quad i > 1 \tag{9}$$

$$\vec{L}_{1,j} = \rho\, \vec{u}_{tot,1,j} \times \Gamma_{1,j}\, \Delta\vec{y}_{1,j} \qquad \text{for} \quad i = 1 \tag{10}$$

The lift for the panels on the leading edge $(i = 1)$ is only influenced by the vortex strength of the same panel while the lift of all subsequent panels $(i > 1)$ along the chordlength is calculated with the vorticity difference $\Delta\Gamma$ to the panel in front. The total velocity present at the panel $\vec{u}_{tot,i,j}$ consists of the global inflow and the induced velocities by all vortex elements:

$$\vec{u}_{tot,i,j} = \vec{u}_{\infty,i,j} + \vec{u}_{ind,wvr,i,j} + \vec{u}_{ind,bvr,i,j} \tag{11}$$

The induced drag can be estimated as well, while the calculation of the total blade drag is not possible as this would require thickness effects being simulated. The summation of the lift for each panel yields the total blade lift, which also allows to calculate the propeller thrust and thrust coefficient.

Obstacle consideration The most interesting obstacles for the scope of this work are a wake-blocking fuselage or wing for VTOL UAV hover propellers (Fig. 1a) and the fuselage or wing behind a rotor in a conventional tractor propeller configuration (Fig. 1b). Due to the nature of the model, it is impossible to consider these elements as a volumetric element. They have to be modeled in similar fashion to the propeller by a thin, possibly twisted and cambered plate. An inherent problem to an obstacle is, that it does not encounter free inflow but will be affected by incoming vortex rings by the propeller. The no-penetration boundary condition, which is also enforced on the obstacle's surface will prevent wake vortex corner points being pushed through the surface of the plate. There are, however two caveats to this assumption:

- Firstly the velocity induced by the bound vortices of the obstacle adheres to Eq. (2) which will only deter an incoming vortex when it is sufficiently close to the surface due to the polynomial increase of the response function.
- Secondly this vortex deflecting behavior is impaired by the desingularization model that is applied with Eq. (4). It will prevent high induced velocity components repelling a vortex filament from a surface.

The surface of the obstacle is therefore modeled with a "ground effect" to mitigate this problem. The ground effect is well understood for helicopter vortex wake structures and is most commonly modeled using the mirror method (e.g. by Griffiths [18] or Johnson [19]). A vortex that is modeled using the mirror method is duplicated below the ground with the reverse circulation $-\Gamma$. The obstacles used in this study are however not an infinite surface such as the ground of a classical ground effect model. Therefore, the obstacle is modeled with a certain mirror thickness that defines an effective mirror region above each obstacle surface. The mirror effect is applied when a vortex filament penetrates this region. Details on the implementation are presented below.

2.2 Implementation

The algorithm presented above has been proven to deliver consistent results by [6] and [10] and [20]. The following sections will adapt this algorithm to enable the flexible and accurate consideration of an obstacle in the propeller wake as well as its flexible integration in the SARF Framework. Several key changes to the well-established VLM algorithm intended to make it more flexible and greatly enhance the simulation capabilities are presented in this chapter.

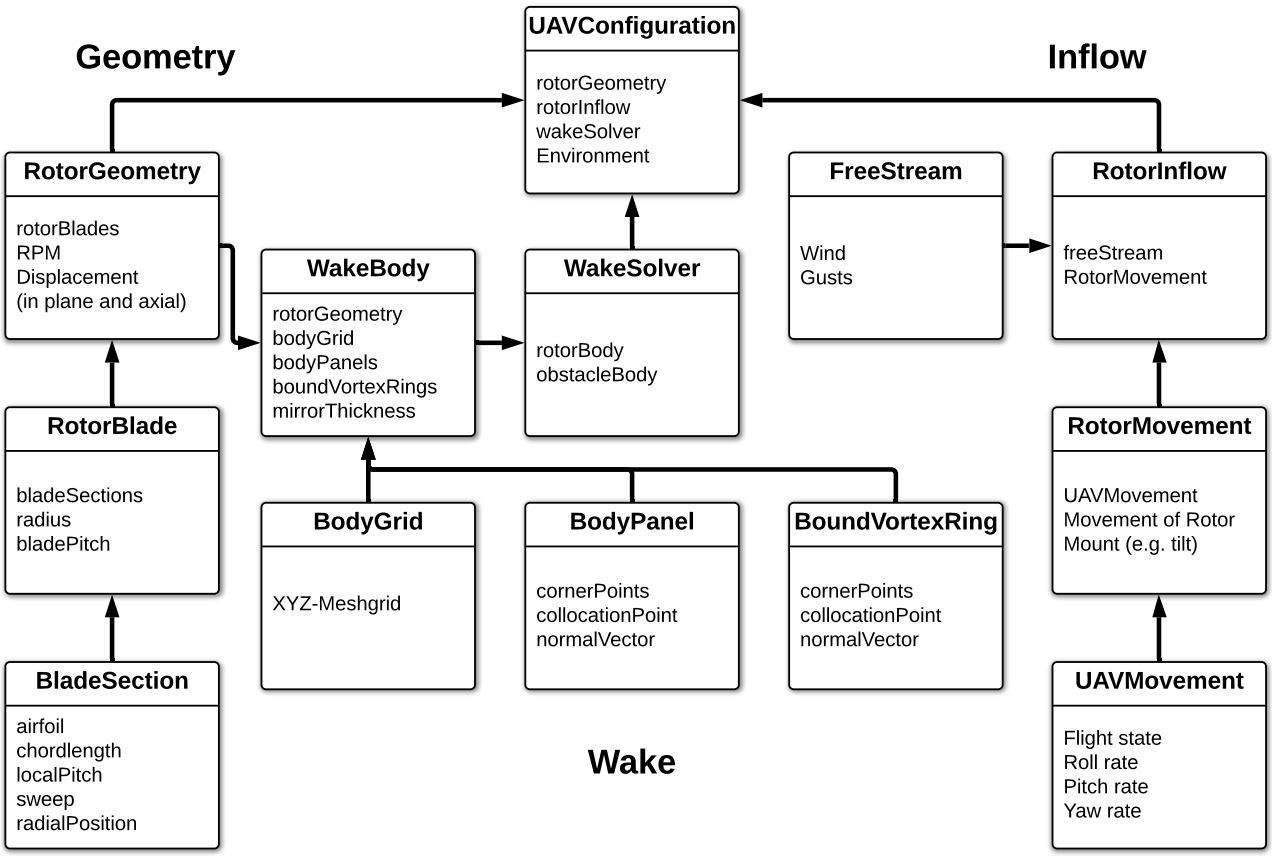

Figure 6 – Hierarchical class structure of SARF Framework

Method integration in SARF Framework & Discretization The model is fully integrated in the modular object-oriented SARF data framework. The existing data structure had to be adapted in order to facilitate an efficient representation of all structures and boundary conditions. All geometric parameters of a relevant body are stored in the left, preexisting part of the classes shown in Fig. 6. The information is retained in a hierarchical way with the airfoil sections as the most basic elements. Multiple sections make up a blade which is part of a rotor.
The right, also preexisting part of the structure in Fig. 6 was developed in [21] and delivers the transient incoming velocity to the rotor depending on UAV movement and external wind and gusts.
This structure can represent an arbitrary rotor and is used to generate the discretized geometry needed for the VLM model. The stored sections are used to derive the panel sheet of the rotor, however, the radial resolution is generally not sufficient as the structure was primarily developed for usage with a BEMT model such as the one described in [9]. Thus the radial resolution is enhanced by linear interpolation of new sections at all radial positions that are required for the panel grid input

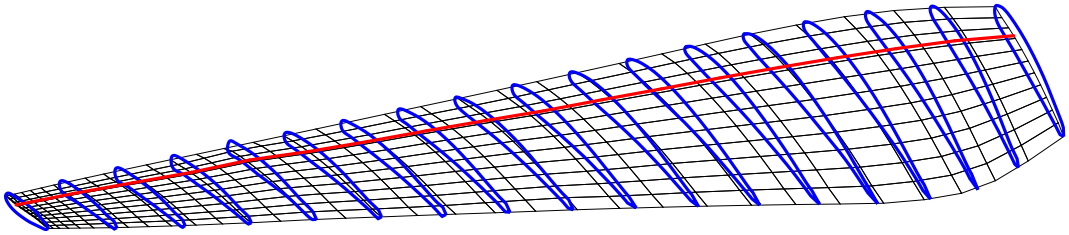

Figure 7 – Discretization of a rotor blade

to the VLM model. The chordwise discretization is derived from the internally stored, pitched airfoil geometry by first calculating the camber line, applying the blade sweep and then discretizing this line as needed.

This gridded camber sheet that has been derived from the main rotor's airfoils is shown in Fig. 7. The original blade sections are depicted in blue with the 25% chord line marked in red. Most grid lines in chordwise direction have no equivalent blue airfoil section, they have rather been interpolated between the two adjacent sections. All airfoils are aligned and the pitch is applied along the 25% chord line. The grid is stored in the newly added "WakeBody" object and defines the object's panels. The vortex rings, collocation points and normal vectors are calculated dynamically based on these panels. The grid shown in Fig. 7 also shows the radial discretization being finer at the blade tip with a sinusoidal spacing that is optionally applied to increase the numerical stability and accurately represent the effects occurring at the blade tips as suggested in [6].

An obstacle that may be present for the calculations is also represented as a "WakeBody" and thus is limited to the variability that can be achieved by the rotor discretization options above. However, the sections can be modeled in any shape. Fig. 8 shows a few of these options. More possible geometries will be shown in the result section below.

The main rotor with an arbitrary number of blades is depicted in blue above an obstacle that is shown in green. Possible obstacle shapes include a second rotor in a coaxial co- or counter-rotating propulsion system (Fig. 8a). This obstacle geometry will be investigated in a follow-up publication due to special aerodynamic effects that have to be considered in this case. A thin plate with various chordlengths and axial as well as in-plane displacement shown in Figs. 8b and 8d can be modeled with only one 'blade' or multiple blades being rotationally symmetrical. This enables the investigation of flat plates and fuselage sections of any shape. Fig. 8c shows a cambered wing as the obstacle. This wing is also modeled as a lifting surface and represents the use-case of vertically tilted hover propeller above a wing or a propeller tractor configuration in front of a wing by increasing the pitch of the wing relative to the propeller (Fig. 1b).

Contrary to the implementation of used in [20], the hub section of the main rotor can be considered for

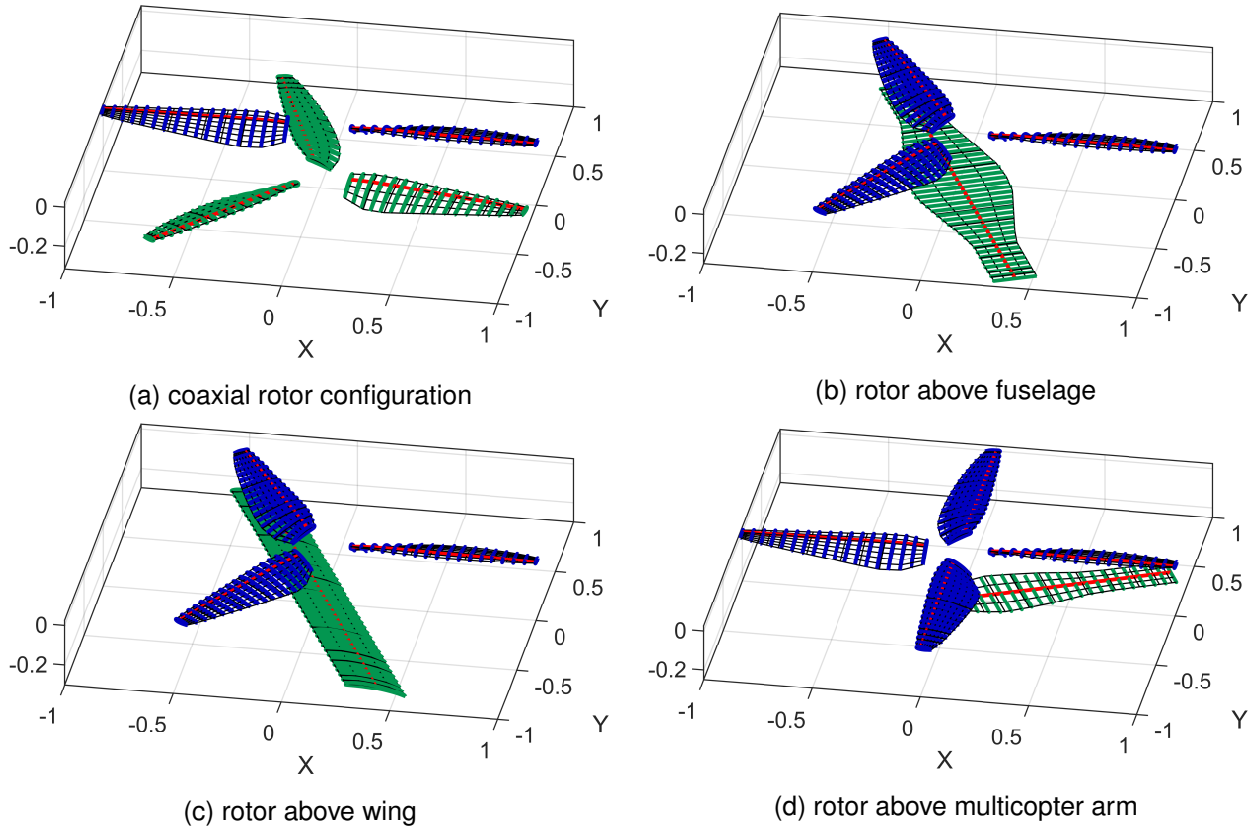

(a) coaxial rotor configuration

(b) rotor above fuselage

(c) rotor above wing

(d) rotor above multicopter arm

Figure 8 – Rotor-obstacle configuration options

two bladed propellers by extending the sections to the rotational axis. This is used in the calculations shown below. It is not considered for propellers with more than two blades. The hub is modeled as a fixed boundary of the blades and thus no root vortex will be generated due to UAV propellers' hubs usually being blocked by the hub section of the propeller.

Definition of the numerical time step Both the rotor and the obstacle are referenced in the "Wake-Solver" class which defines all properties and functions needed for the model to run. It compiles all data from the various storage classes to use in the algorithm.
The global time step has to be determined during the initialization phase of the algorithm. The size of the wake panels is dependent on the inflow velocity, the rotational speed and the length of one time step. It is important for the numerical stability of the time marching algorithm that the wake panels are of appropriate size. It should ideally be similar to the size of the bound vortex panels which only depends on the discretization of the blade geometry and should furthermore roughly resemble a square.
In order to automatically consider the discretization scheme of the propeller an approach following the one suggested by [11] is taken. It defines two characteristic variables L_c and U_c:

- L_c is the characteristic cell length of the bound vortex rings. It is measured in chordwise direction at $r = 0.75R_{Tip}$ which is the most commonly used radius to define characteristic propeller parameters.
- U_c is defined as the characteristic inflow velocity which is composed of the global inflow and the rotational velocity $U_c = |\vec{u}_\infty + \Omega r|$. It is also measured at $r = 0.75R_{Tip}$.

The global time step is determined accordingly:

$$\Delta t = CFL \frac{L_c}{U_c} \tag{12}$$

CFL hereby denotes the CFL factor which is widely used in CFD analyses. As the model presented here is using an explicit forward Euler time marching numerical scheme, a CFL number < 1 is chosen. Both the propeller and the obstacle may move with a rotational frequency Ω. Each of these structures as well as their bound vortices and panels have to be rotated by $\Delta\phi = \Delta t\, \Omega$. The objects will only rotate around the center of the coordinate system as any movement of this propeller fixed coordinate system is represented in the transient inflow $\vec{u}_\infty$ that is delivered by the "Inflow" class-group presented above. It is not possible to simulate relative movements between the propeller and the obstacle other than an individual rotational frequency.

Matrix representation The classical VLM algorithm will form a new wake vortex row for each time step. This sheet of vortex rings will not break up or dissipate as the model is based on potential flow with no internal friction. Each new row thus increases the number of vortex filaments that have to be considered in Eq. (7) with the AIC matrix growing in both dimensions which would lead to an exponential increase in computational effort as the number of time steps increases.
To prevent this and to consider the decreased influence of old wake vortices on the propeller, the wake is cut off after a predefined vortex age which is in general less than the total number of time steps that are calculated until the wake converges. This enables the pre-allocation of all matrices that are needed during the calculations. Values are added to these matrices in a circular manner with a revolving index pointer indicating the current row that is used by the newly shed vortex row. This prevents a shifting of the matrix contents and is thereby saving computational effort.

Biot-Savart-Law calculation The vortex rings seen in Fig. 2 are arranged in a vortex sheet. The center vortex rings of the structure are characterized by two vortex filaments of neighboring vortex rings having the same but reversed start- and end-points. This can be used to reduce the computational load using the separation between the geometric influence and the vortex strength mentioned

in Eq. (6). The influence coefficients $a_{i,j}$ are calculated only once for these vortex filament pairs which reduces the amount of coefficients that need to be calculated to roughly $2/3$ due to the vortex sheet boundaries having no overlapping vortex filaments. As the calculation of Eq. (7) is the computationally most expensive part of each time step, this speeds up the algorithm performance considerably.

Vortex separation and fusion The goal of assessing the interference between a main object and an obstacle yields additional challenges that need to be addressed in order to improve the simulation accuracy and achieve rapid simulation convergence.
A vortex filament defined between two wake corner points will persist until these corner points are removed from the computational domain due to their age. Relative movement between these two corner points will lead to a contraction and extension of the individual vortex filaments. This is a sufficient wake approximation as long as the wake is unobstructed. In the presence of an obstacle, this behavior has to be adapted.
While approaching an obstacle, it is possible for one corner point to flow above the obstacle geometry while the other corner point will flow below the obstacle which would lead to a vortex filament being defined straight through the obstacle body which is not physically sound.
When these mesh points are separated in such a way it is sensible to cut the vortex sheet and remove the affected vortex filament from the computation. This is one of the key improvements on the established VLM algorithm that is presented in this paper. The effect is shown as a 2D view in Fig. 9 where a wing element depicted in orange is affected by a perpendicular incoming velocity indicated by the purple arrow. The wing element produces a three dimensional wake vortex sheet shown in blue with both outer edges exhibiting tip losses and the subsequent roll-up of the vortex-

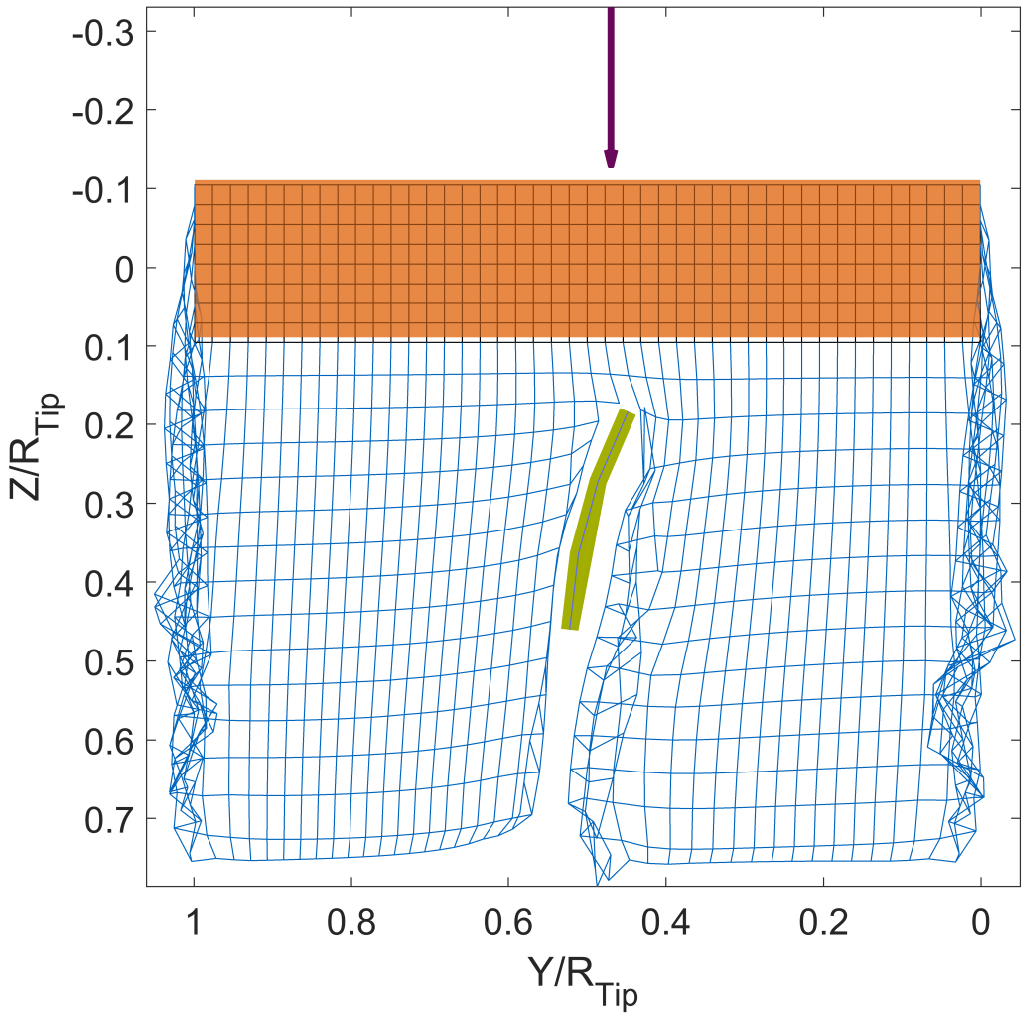

Figure 9 – Sample plot for vortex sheet separation

sheet clearly visible.
The vortex sheet is met by another cambered wing element shown in green that is oriented perpendicular to the orange wing and is a continuous body that extends above and below the viewing plane. This obstacle element is also producing a wake vortex sheet on it's trailing edge that is not shown in the figure. It however influences the main vortex sheet's trajectory behind the obstacle. Vortex filaments of the main body's vortex sheet whose start- and end-points fall on different sides of the wing obstacle are cut which results in the whole vortex sheet being separated by the green wing. The separated vortex sheets then continue traveling downward along and around the obstacle geometry. The edges begin to form the expected roll-up of an exposed vortex sheet edge as the traveled distance increases, especially on the high pressure side on the right of the obstacle.
It can be observed in the figure, that the influence area which causes the vortices to separate extends some distance to the front of the obstacle which is inspired by the effects experienced by potential flow around an arbitrary body. Similarly it is also possible for the severed vortex sheet to be merged again when the obstacle has been passed and the vertices have not diverged too far apart.
Numerically, this is implemented by deactivating the vortices while they are in a severed state. The matrix entries representing the start- and end-vertices are still filled, however the vortex strength Γ is set to zero. This allows to preserve of the vertex correlations forming the individual filaments while removing the influence of the severed vortices from the computation. However, the initial vortex strength Γ is also saved in order to possibly merge the vortices back together after the passage of the obstacle.
The separation process relies on having a small computational cost when determining, which vortices are cut by an obstacle as it would otherwise slow down the whole simulation significantly due to this decision being required for every vortex in every time step. The vortex will be severed when its start- and end-points reside on different sides of an obstacle geometry. Both points defining an individual vortex filament are therefore assessed for each vortex in the wake region. The three step process for this decision is outlined in Fig. 10.
As a first step, an influence region of a certain influence thickness t_{infl} is defined which extends in normal direction of the obstacle surface. This region is defined separately above and below the surface. The normal direction of each bound vortex ring is known from Eq. (8) and can be used to define these two regions. This step is not performed for each time step. The influence region is rather calculated during the algorithm initialization procedure and the influence region is subsequently moved in accordance with the geometry for all time steps. Vortices outside of this influence region will not be further assessed for vortex separation.

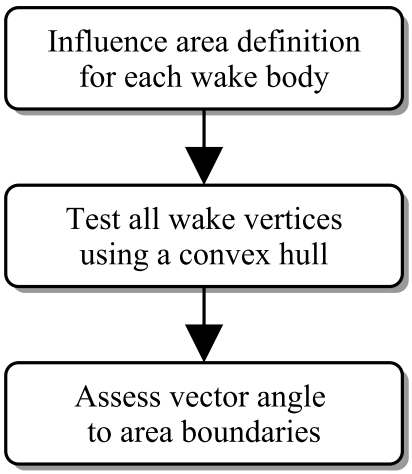

Figure 10 – Testing for residence in influence region

Secondly, a convex hull is calculated from the boundary points of each region for each body in the computational domain. Testing for points residing in this convex hull is done by converting all facets of a region into linear inequalities and determining whether a point resides on the same side of all inequalities. In this Matlab implementation, an external function providing this capability is used [22]. This function works similar to a bounding box test and can quickly filter all vertices that are clearly outside the influence region. It will, however, also produce a certain amount of false positive indicators for vertices near cambered or otherwise irregularly shaped bodies which can only be poorly approximated with a convex hull.
Hence the third step consists of assessing all query points q_i that have been positively tested by the convex hull function above. Each influence region on each side of the obstacle is split in an upper and a lower surface as shown in Fig. 11 with the lower surface being equal to the original obstacle surface and the upper surface being equal to the influence area boundary. Next, a vector $\vec{v}_1$ and $\vec{v}_2$ is calculated from each query point q to both surfaces. Both vectors are defined being the shortest

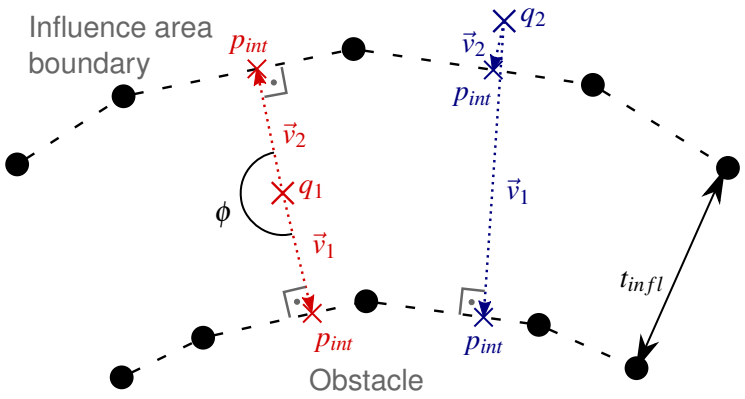

Figure 11 – Query points q_1 between and q_2 outside of Influence Layers

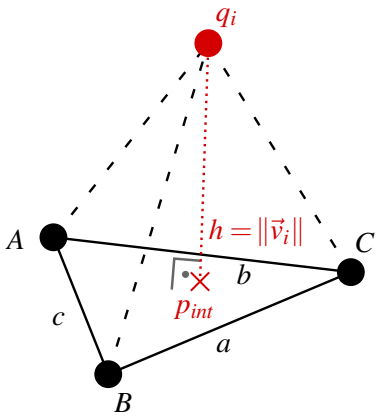

Figure 12 – Tetrahedron Schematic to determine h

perpendicular connection between q and the respective surface.
The angle ϕ between these vectors pointing to the upper and lower surface is then determined using Eq. (13) with the vector from the query point q to the obstacle surface as $\vec{v}_1$ and the vector to the influence area boundary as $\vec{v}_2$. This angle will be close to $180°$ for points inside the influence region and close to $0°$ for points that are outside which enables an efficient way of determining residence in the influence region.

$$\phi = 2\arctan\left(\frac{\left\|\left(\vec{v}_1\|\vec{v}_2\|\right)-\left(\|\vec{v}_1\|\,\vec{v}_2\right)\right\|}{\left\|\left(\vec{v}_1\|\vec{v}_2\|\right)+\left(\|\vec{v}_1\|\,\vec{v}_2\right)\right\|}\right) \tag{13}$$

Calculating these vectors $\vec{v}_i$ with a small computational effort is paramount to the overall algorithm efficiency. They have to be determined as vectors between the query point q and the surface, while the latter is only represented by discrete grid corner points of the geometry.
Fig. 12 shows, that the intersection point p_{int} between the vector $\vec{v}_i$ and the surface will be within the closest triangle formed by corner points $[A,B,C]$ on the surface grid. Furthermore, $\vec{v}_i$ needs to be perpendicular to the surface, in this case of a discretely defined surface it needs to be perpendicular to the triangle $\triangle_{[A,B,C]}$. An irregular tetrahedron is defined by this base triangle and q_i in order to determine $\vec{v}_i$. The height h of the tetrahedron which is equal to $\|\vec{v}_i\|$ is calculated by solving the pyramid volume formula for height:

$$h = \frac{3V_0}{A_0} \tag{14}$$

A_0 represents the area of the base triangle which is given by Heron's Formula Eq. (15) with the semi perimeter $s = {}^{(a+b+c)}/_2$. The tetrahedron volume V_0 is calculated by Eq. (16) using the scalar triple product of the vectors from q to $[A,B,C]$ each:

$$A_0 = \sqrt{s\,(s-a)\,(s-b)\,(s-c)} \tag{15}$$

$$V_0 = \frac{\left|\overrightarrow{(A-q)}\left(\overrightarrow{(B-q)}\times\overrightarrow{(C-q)}\right)\right|}{6} \tag{16}$$

Multiplying the scalar height h with the triangle's normal vector $\vec{n}_{\triangle_{[A,B,C]}}$ yields the perpendicular vector $\vec{v}_i$ between the surface and q_i.
The closest triangle $\triangle_{[A,B,C]}$ that is used here needs to be determined in a separate step for the formula above to work. Figure 13 depicts one possible triangulation of a 3D-surface grid projected on the 2D figure seen from above with 6 triangles that share the closest grid collocation point cp_c.

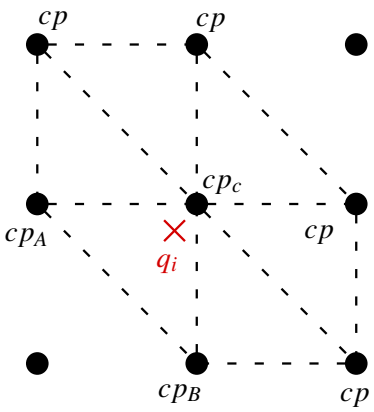

Figure 13 – Top view of surface triangulation and query point q_i

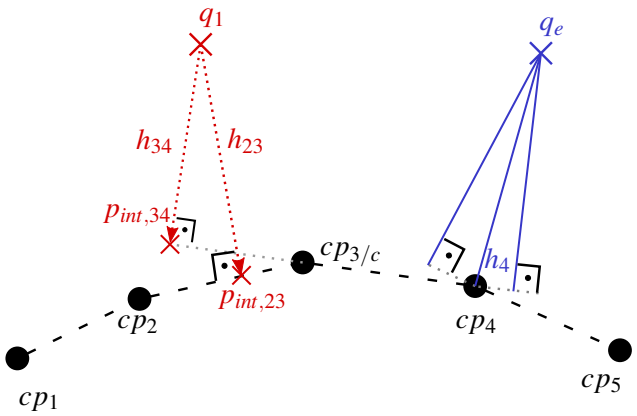

Figure 14 – Side view of 2D intersection algorithm

Marked with a cross is a projection of the query point q_i on the surface. cp_c is the grid point with the smallest geometric distance to the query point q_i and is easily determined from the point coordinates.

$$\overrightarrow{cp}_c - \overrightarrow{q_i} = \min_{\forall cp_j \in cp} \left(\overrightarrow{cp}_j - \overrightarrow{q_i}\right) \tag{17}$$

The discretization length in chordwise and radial direction is allowed to be vastly different in the model presented in this paper. Additionally, the discretization length might be irregularly distributed and variable over the obstacle geometry. This flexibility needs to be considered due to the aforementioned extension of the influence area in front of and behind the obstacle. Subsequently, the $\triangle_{[A,B,C]}$ is not always defined by the three geometrically closest points to q_i. It will, however always consist of the corner point that is closest to the query point: cp_c.
Further complications arise because two adjoining triangles on a three dimensional surface are in general not oriented in the same direction which can lead to kinks between the triangles. Figure 14 shows this challenge in a simplified form for query point q_1 depicted in red by showing the corresponding 2D-Problem where the tetrahedron mentioned in Fig. 12 is reduced to a triangle and the triangles $\triangle_{[A,B,C]}$ of the surface are depicted as line segments. Point $cp_{3/c}$ is the closest surface point to q which leads to the calculations mentioned above being evaluated for line segments $[cp_2, cp_3]$ and $[cp_3, cp_4]$. Eq. (14) produces a valid result both for h_{23} and h_{34}. However, h_{34}, while perpendicular to line $[cp_3, cp_4]$, will lead to the calculation of an interception point $p_{int,34}$, that is not located on the surface and not within the line segment $[cp_3, cp_4]$.
Transferring back to the 3D-Problem, this necessitates all 6 triangles depicted in Fig. 13 to be evaluated. The intersection point p_{int} is determined for each triangle and then checked whether it is enclosed in the base triangle using barycentric coordinates [23]. Two edges of each base triangle are used as unit vectors to construct a barycentric coordinate system. The intersection point's coordinates transformed to the barycentric coordinate system tell, if p_{int} is within the base triangle when all of the following assumptions hold for both barycentric coordinates u and v of p_{int}:

$$p_{int} = p(u,v) \in \triangle_{[A,B,C]} \text{ for } \begin{cases} u \geq 0 \\ v \geq 0 \\ u+v < 1 \end{cases} \tag{18}$$

This will yield the desired triangle $\triangle_{[A,B,C]}$ that is needed in Eq. (14) to determine the vector $\vec{v}_i$. However, some cases might occur that will not yield any intersection point using this process. This case is illustrated in Fig. 14 in blue for query point q_e on a convex surface. The perpendicular intersection line will yield a point that is outside of the line segment for both segments $[cp_3, cp_4]$ and $[cp_4, cp_5]$. In this case the resulting interception point p_{int} is equal to surface point cp_4 and the line h_4 is not perpendicular to any line segment. The equivalent 3D-case for this situation results in two options:

1. The interception point p_{int} is located on the edge of a triangle. This edge runs from cp_c to any adjoining corner point that is reachable via a dashed line in Fig. 13.

2. The interception Point p_{int} is equal to cp_c.

Testing for these two cases is done by evaluating the correct edge out of all edges adjacent to cp_c shown in Fig. 13. A small step along the correct edge will be closer to q_3 than cp_c and closer than the same step along all other edges. Alternatively if no step along an edge is closer than cp_c, case two is returned. In the first case, a simple golden ratio minimum search as first proposed by [24] is used to determine the closest point between the edge and q_3. The minimum search along an edge could also be replaced by simple geometric calculations, however, those would need to consider further special cases such as query points way to the side of the tested finite surface.
The algorithm described in this chapter is able to determine the perpendicular vector between the boundary surfaces of the influence area and a query point. These vectors are used for Eq. (13) and the angle ϕ is used to quickly determine query point residence in an influence region. Vortices whose start- and end-points reside on both sides of an obstacle will be severed just as depicted in Fig. 9 with the wake being separated by the wing element.
This process is able to consider an irregularly discretized, arbitrarily spaced, twisted and deformed grid in three dimensional space and thus is ample to consider all future obstacle geometries that are planned to be implemented for the wake model.

Mirror Method A vortex filament that falls within the mirror region that was introduced above has to be reproduced below the obstacle surface. The mirror region is defined in an analogous way to the influence region mentioned above: Each obstacle surface is associated with a certain mirror thickness. This thickness is applied in the local normal direction of the surface which defines the mirror region. The mirror region is in general smaller than the obstacle influence region. Thus, all vertices that fell into the influence region are tested whether they are also located inside the mirror region using the process described in the previous chapter.
The perpendicular vector to the obstacle surface that is determined as a byproduct in this process is then duplicated below the surface to define the position of the mirrored vortex element. This test will be performed for each vertex, however a vortex is only mirrored when both it's start- and end-point fall within the mirror region.
The ground effect that is the basis for this functionality is usually applied to an infinite ground floor. However, a vortex moving around an obstacle with finite dimensions can also reach a position below the obstacle which is why this mirror method is applied both above and below the obstacle surface. The mirrored vortices of both sides are, however, applied separately which implies that a vortex filament above the surface will not be influenced by a mirrored virtual vortex from a filament below the surface.
The consideration of these mirrored vortices enables a smooth flow of vortex filaments around an obstacle while adhering to the no-penetration boundary condition imposed on the surface.

3. Computational Results and Application

Validation of the model is carried out in comparison to various measurement data. The first calculations compare the analysis of a single rotor without any obstacle to measured data. The subsequent assessment will investigate the effect of an obstacle on the propeller performance.

Static thrust The first validation calculation has been carried out using the widely known Caradonna-Tung rotor with static thrust measurement data published in [26]. Fig. 15 shows a comparison of the model presented in this paper (SARF) with other simulation tools: Dust, FlowLab and VSPAero. The global pitch of the propeller blades and the rpm are varied. More details on these comparative studies

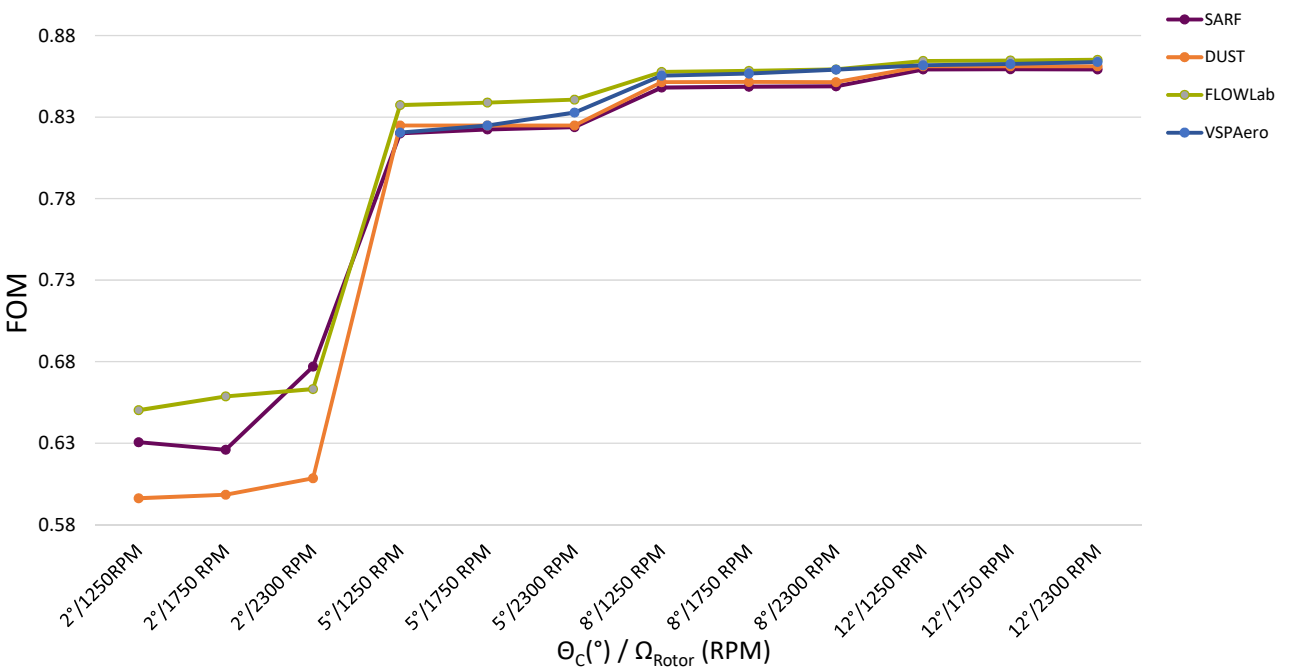

Figure 15 – Comparison of SARF wake simulation with various simulation tools [25]

is presented by Perdolt in [25]. The Figure on Merit (FOM) has been calculated with the formula:

$$\text{FOM} == \frac{\frac{C_T{}^{3/2}}{\sqrt{2}}}{\frac{\kappa C_T{}^{3/2}}{\sqrt{2}} + \frac{\sigma C_{d_0}}{8}} \tag{19}$$

The SARF model can accurately predict the rotor FOM for higher global pitch angles and all rpm. Higher pitch angles correspond to a higher thrust coefficient C_T. The differences shown on the left side of the graph imply, that the accurate simulation of a propeller operating with a small C_T is challenging for all tools.

Inclined Inflow Kolaei [27] has measured a T-Motor 18x6.1 propeller whose geometry is described in detail in [28]. The tests have been conducted under various advance ratios and inflow angles θ ranging from perpendicular inflow ($\theta = 0°$) to perpendicular backwards flow ($\theta = 180°$). These measurements have been simulated for inclined inflow angles in the range of $\theta \in [0°, 85°]$. The simulation of backwards inflow has not produced sensible results. The C_T-Values have been calculated using the formula:

$$C_T = \frac{T}{\rho A \left(\Omega R_{Tip}\right)^2} \tag{20}$$

The advance ratio is calculated using the perpendicular inflow velocity $V_\perp$ which is parallel to the propeller axis.

$$J = \frac{V_\perp}{\Omega R} \tag{21}$$

Fig. 16a shows the wake structure of the propeller operating at 5000 RPM under an inclined inflow with $\theta = 60°$. The inflow vector is shown above the propeller. The wake vortex sheets originating from the propeller can be clearly distinguished and the distinctive tip vortex roll-up is present. Further downstream the wake vortex sheets are breaking up and mixing into the far wake vortex area. Figs. 16b to 16d show the thrust coefficient of the propeller under inclined inflow for 3000, 4000 and 5000 rpm with the dotted line representing measured data, while the solid line represents the simulation.

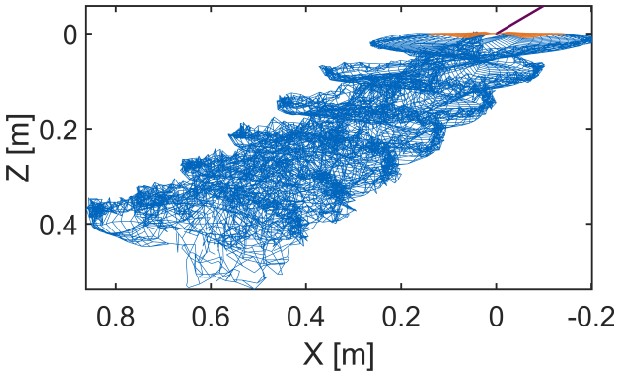

(a) Side View of Wake with $\theta = 60°$

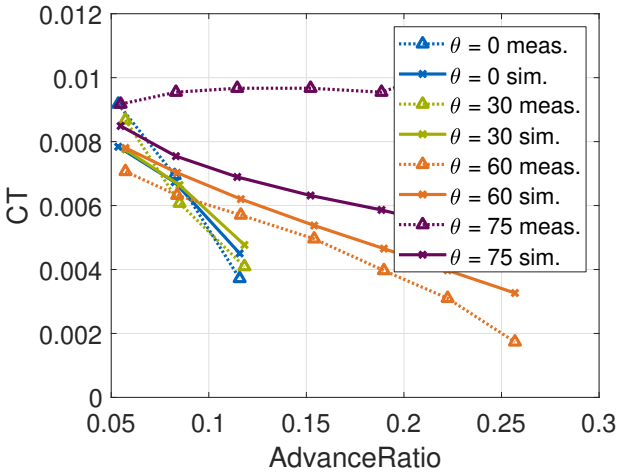

(b) C_T at 3000 RPM

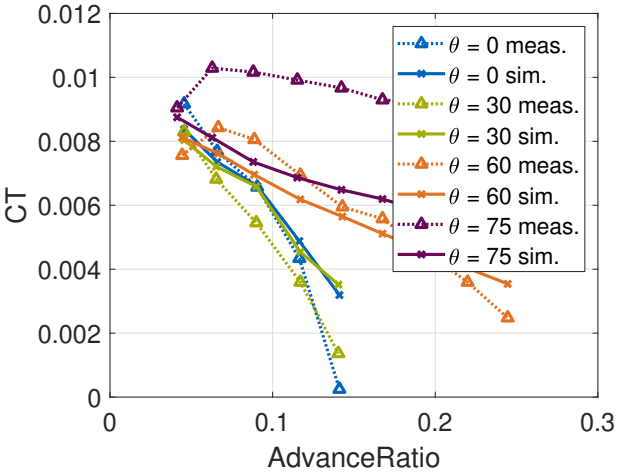

(c) C_T at 4000 RPM

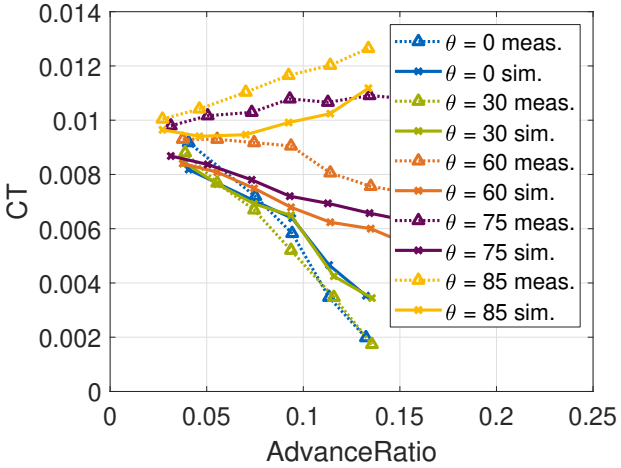

(d) C_T at 5000 RPM

Figure 16 – Comparison with measurements by Kolaei [27]

The simulation can successfully capture the trend of C_T for a wide range of inclination angles. An inclination angle of $\theta = 75°$ produces diverging results while an angle of $\theta = 85°$ can again capture the overall trend of C_T. The relative difference between the measurements and the simulated data is less than roughly 10% for most flow states except for $\theta = 75°$. Similarly to the findings in Fig. 15, the model has difficulties predicting small C_T correctly which occur with higher advance ratios.

Ground effect The next simulation assesses the interaction between a propeller and the ground. This effect can be simulated due to the mirrored vortices described above. The ground is simulated as a big, flat obstacle. Fig. 17 shows the propeller with the ground plate and the wake vortices. The wake that is produced by the propeller moves to the ground plane under the global inflow coming straight from above. The wake contraction and subsequent drift in radial direction near the ground can be seen below the propeller. Wake vortices will accumulate above the ground plate and extend to the side. The ground plane is not defined with infinite dimensions as it is modeled as an obstacle. Subsequently, the wake vortex rings can be seen flowing around the edges of and below the obstacle where they will be cut due to the wake separation effect.
Cai [29] has measured the static thrust performance of an APC 11x5.5 thin electric propeller when operated in ground effect. The propeller geometry is also described in [28]. The propeller was therefore mounted with various distances to a ground plate and the thrust coefficient C_T normalized by the unobstructed C_{TOGE} (Out of Ground Effect) was noted. This enables the assessment of the changes in propeller performance due to ground proximity.
Fig. 18 shows the measurements and it's analogous simulation results. C_T/C_{TOGE} is shown over h/D

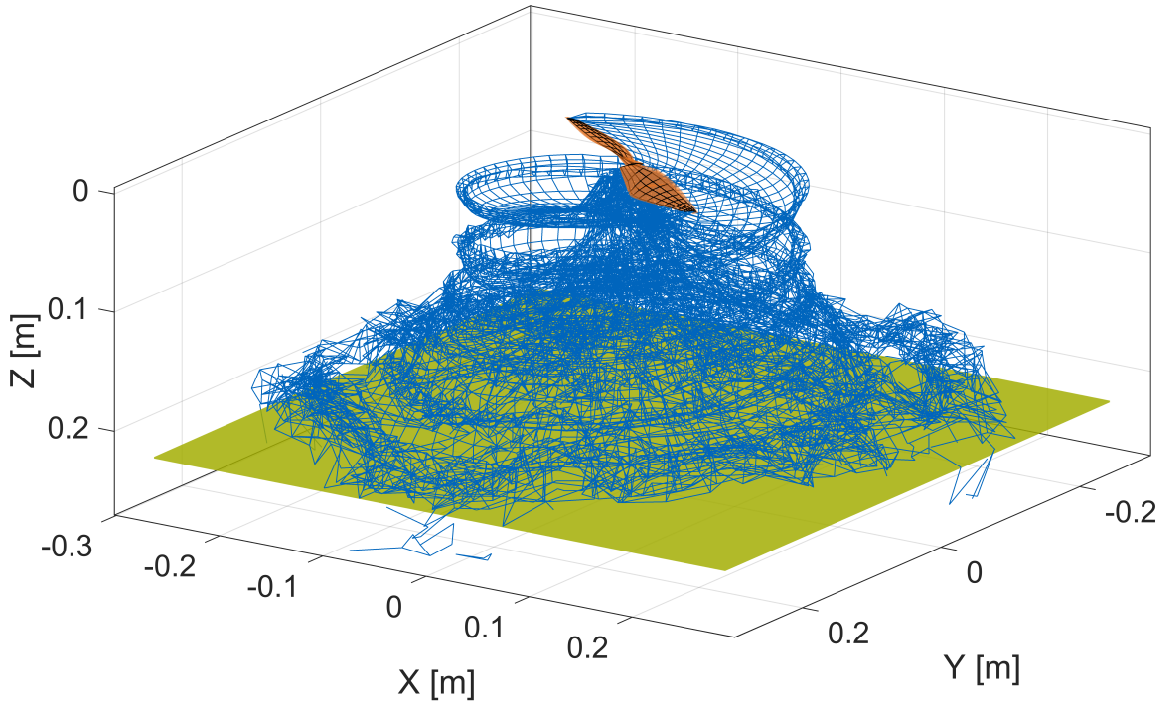

Figure 17 – Calculation of Ground Effect

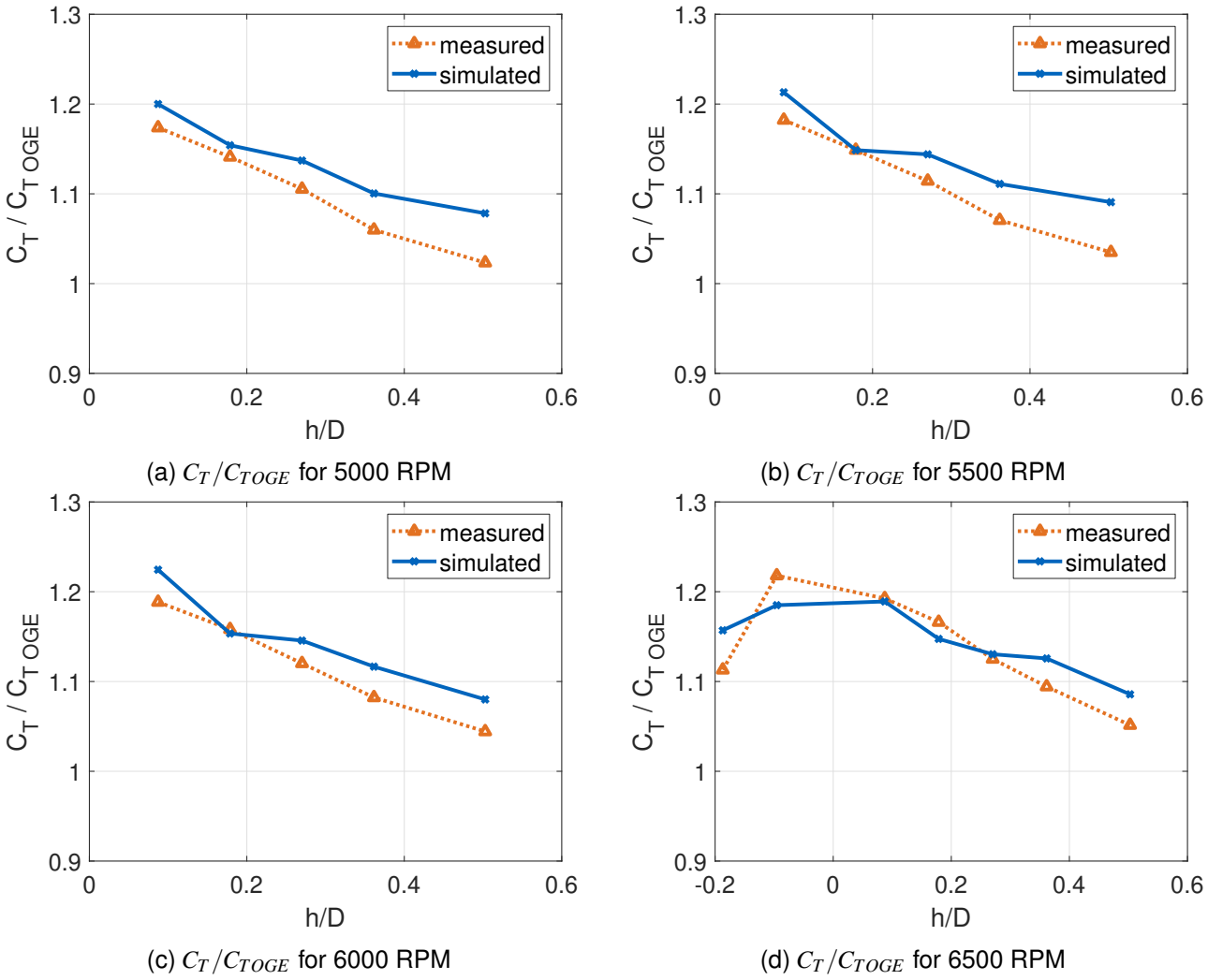

(a) C_T/C_{TOGE} for 5000 RPM

(b) C_T/C_{TOGE} for 5500 RPM

(c) C_T/C_{TOGE} for 6000 RPM

(d) C_T/C_{TOGE} for 6500 RPM

Figure 18 – Ground effect: C_T/C_{TOGE} over h/D measured by Cai [29] on an APC 11x5.5 thin electric propeller

which is the ground distance normalized by the propeller diameter. This simulation also successfully captures the trend of the measurements for all RPM. The slope of increase C_T/C_{TOGE} for a smaller ground proximity is very similar to the measurements, while the actual effect of the ground is slightly overestimated.
The h/D ratio shown in Fig. 18d extends to the negative side which corresponds to the propeller oriented in ceiling effect. The measurements by Cai provide further data on this flight state. However, only two test cases have been assessed due to the model not providing an accurate representation of this flight state. The effect of the propeller pulling and accelerating air along the ceiling in it's upstream area is not modeled.
The mean error in C_T/C_{TOGE} between the simulation and the measurements over all test cases with a positive h/D ratio is 2.1%. These results show that the takeoff procedure of a UAV can successfully be simulated and can provide valuable input to the overall aircraft design input.

Blockage through obstacles A focus of this model is placed on the prediction of a propeller operating with an obstacle in the slipstream. Measurement validation data for this configuration is scarce. Cai also published measurements of the propeller performance operating in partial ground effect which is used for validation. [30]
The experimental setup is similar to the test cases presented above. One propeller is mounted above a circular flat plate with the center below the propeller axis. The tested propeller is an APC 17x7 thin electric propeller operated at 6000 RPM. It's sectional geometry is given in Fig. 20a. The plate radius is defined by the blockage ratio.

$$B = \frac{r_{plate}}{r_{tip}} \qquad B \in [0.5, 0.75, 1] \tag{22}$$

Fig. 19 shows the setup that was recreated within the simulation. The vortices created by the propeller are obstructed by the circular base plate. They are pushed outward which is clearly visible in the lower part of the figure. Afterwards, they are flowing around the plate while interacting with its vortices and the wake generated by it. Vortices wrapping around the plate can be seen being cut by the separation algorithm.
Figs. 20b to 20d compare the measured and simulated change between the C_T of an unobstructed to an obstructed propeller for different obstacle sizes. The results show a strong fit starting at a certain

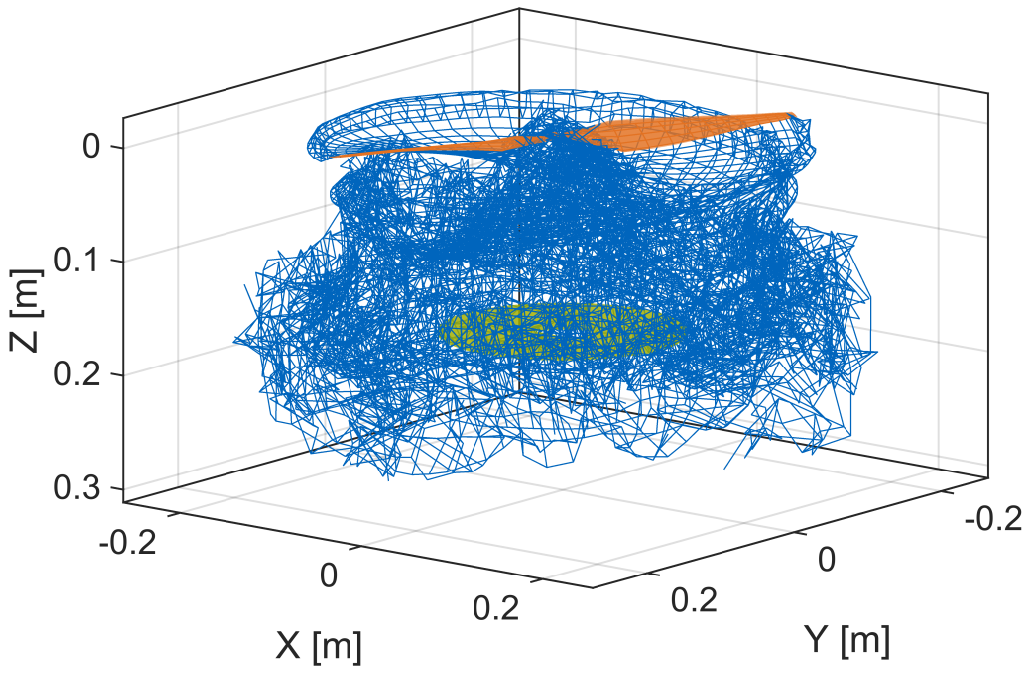

Figure 19 – Computational setup for $B = 0.5$ and $h/D = 0.4$

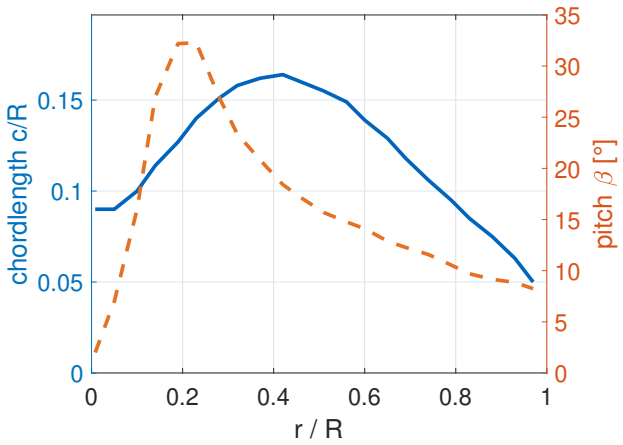

(a) Pitch and chordlength distribution of APC 17x7 thin electric propeller

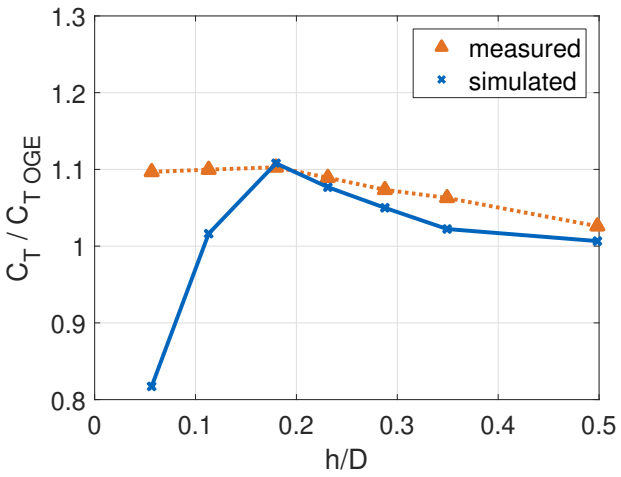

(b) C_T/C_{TOGE} for $B = 0.5$

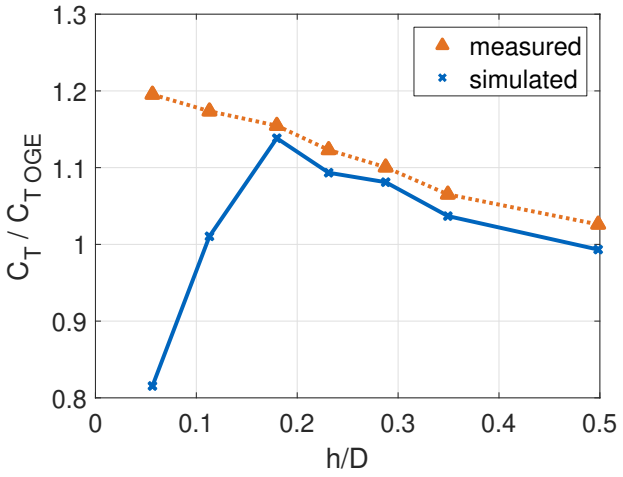

(c) C_T/C_{TOGE} for $B = 0.75$

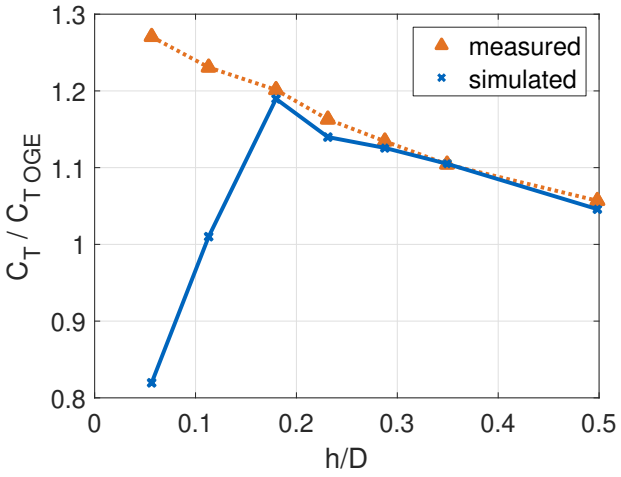

(d) C_T/C_{TOGE} for $B = 1$

Figure 20 – Partial ground effect: Propeller geometry and C_T/C_{TOGE} over h/D measured by Cai [30] on an APC 17x7 thin electric propeller

distance of $h/D > 0.15$. The mean error between the measurements and the simulation for $h/D > 0.15$ is 1.7%. The reason for the simulation results to diverge from the measurements for a close obstacle placement is due to the wake vortices produced by the obstacle heavily influencing the bound vortices on the propeller blades that are used to determine C_T. The obstacle plate is fully stalled due to the perpendicular inflow while the model is unable to accurately predict stall behavior. The simulations of an infinite ground plate above did not show this problem due to the obstacle's wake vortices only being produced at the borders of the geometry farther away which causes less interference..

Application to configurational studies The simulation framework can be used to carry out parameter studies on design trade-offs where variations in the component arrangement of a UAV can be assessed and compared with a relatively low effort and computational cost. A high number of configurations can be automatically evaluated since no manual meshing activity is required for an individual computation. This is demonstrated in Fig. 21 where the placement of a hover propeller operating at 5000 RPM is varied to reside at the nose and in the middle of a UAV fuselage that is represented by a cambered geometry. The UAV is in transition flight where the inflow vector is tilted slightly to the front.
The different flow states of the vortices around the fuselage can be clearly distinguished. The blue wake vortices can be seen being blocked by the fuselage. The lower vortex sheets have been cut by the fuselage and have subsequently flown past. This is in contrast to many classical VLM models where vortices blocked by an obstacle are either stretched and unable to flow past it or are simply

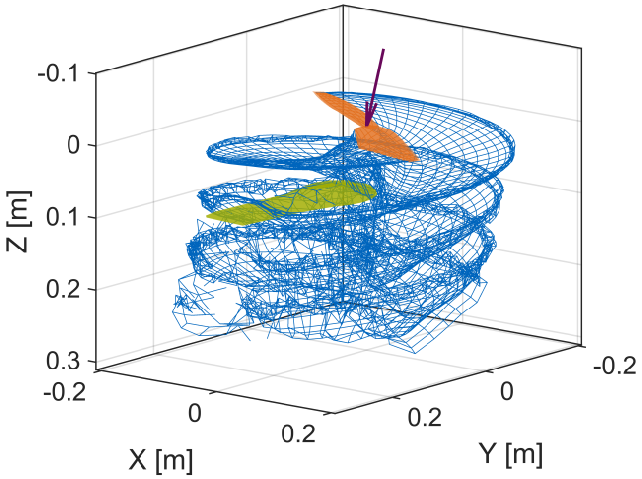

(a) Propeller at fuselage nose

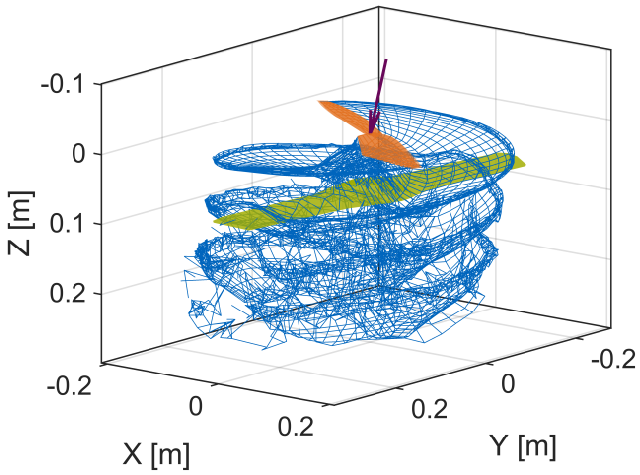

(b) Propeller at mid-fuselage

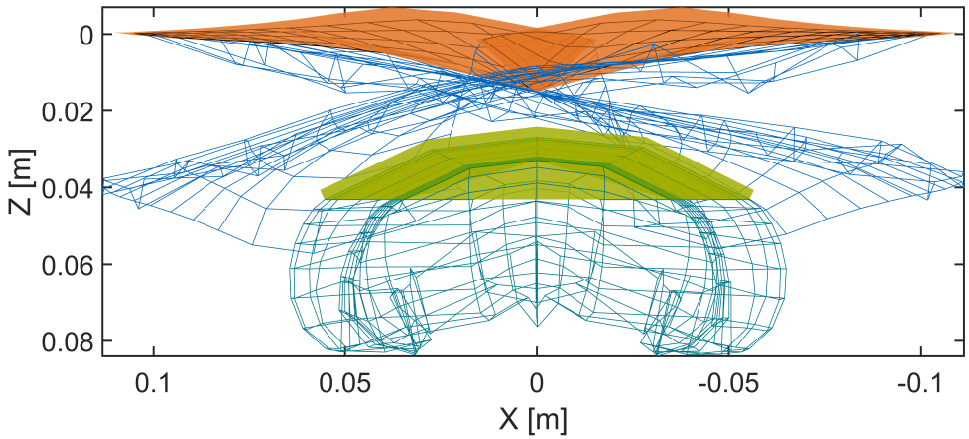

(c) Detail view of wake vortices

Figure 21 – Tractor hover propeller above a UAV fuselage

flowing through the obstacle. The wake that is produced by the fuselage is interacting with the propeller wake but is not shown in the upper two figures. Fig. 21c shows a detail view of the wake vortices after the calculation of 10 time steps and also shows the wake that is produced by the fuselage. In this case, the wake is produced on all sides as the obstacle is no lift generating surface with a clear leading- and trailing edge.

This sample study also shows one core weakness of the current model, which is the inability to accurately handle volumetric obstacles other than cambered blades and sheets. The vortex sheet separation algorithm can currently only separate vortices where one end is on either (upper and lower) side of an obstacle. Vortices with both ends on the upper side as visible in Fig. 21a will not be cut and can therefore still run through the obstacle geometry. Furthermore, the model is not yet able to predict stall and flow separation behavior as the wake-shedding elements have to be explicitly defined for each calculation. The power requirements of a propeller can currently not be derived due to the inherent limitations of the VLM theory. It is planned to couple a separate power estimation algorithm with the solver and to handle volumetric obstacles in a future publication.

4. Conclusion

In conclusion, this model shows the capabilities of a flexible UAV simulation environment where design-studies can be carried out with respect to geometric variations of the configuration and various flow states. The automatic mesh generation requires minimal user input which makes the model well suited for automated design sweeps. The mirror effect applied on all objects greatly improves the vortex behavior near obstacles while the vortex separation algorithm enables a more realistic interaction of the vortex sheets with another object.

The absolute accuracy of the thrust prediction of a propeller that is derived from the vortex structure is promising while the relative comparison of different flow states and geometries provides strong insights on the mutual interactions between a propeller and an obstacle.

5. Contact Author Email Addresses

Moritz Thiele	Moritz.Thiele@tum.de
Dimitrios Salassidis	Dimitrios.Salassidis@web.de
Mirko Hornung	Mirko.Hornung@tum.de

6. Copyright Statement

References

[1] Landgrebe AJ. The wake geometry of a hovering helicopter rotor and its influence on rotor performance. Journal of the American Helicopter Society, Vol. 17, No. 4, pp 3–15, 1972. doi: 10.4050/JAHS.17.3.

[2] Giovanetti EB. Optimal Aerodynamic Design of Conventional and Coaxial Helicopter Rotors in Hover and Forward Flight. Dissertation abstracts international, volume: 77-05(e), section: B.; 193 p. edition, ProQuest Dissertations And Theses, 2015. ISBN 9781339318240.

[3] Panayotov F, Dobrev I, Massouh F and Todorov M. Studying the wake contraction of the flow-field of a rotor in hover. MATEC Web of Conferences, Vol. 133, No. 2, pp 01009, 2017. doi: 10.1051/matecconf/201713301009.

[4] Veldhuis LLM. Propeller Wing Aerodynamic Interference. Dissertation, Delft University of Technology, Delft, 2005. URL https://repository.tudelft.nl/islandora/object/uuid:8ffbde9c-b483-40de-90e0-97095202fbe3?collection=research.

[5] Marretta ARM, Davi G, Lombardi G and Milazzo A. Hybrid numerical technique for evaluating wing aerodynamic loading with propeller interference. Computers & Fluids, Vol. 28, No. 8, pp 923–950, 1999. ISSN 00457930. doi: 10.1016/S0045-7930(98)00055-3.

[6] Abedi H, Davidson L and Voutsinas SG. Development of free vortex wake method for aerodynamic loads on rotor blades. In European Wind Energy Association annual event 2014 (EWEA 2014), Red Hook, NY, 2014. Curran. ISBN 9781510815735.

[7] Cao Y, Lv S and Li G. A coupled free-wake/panel method for rotor/fuselage/empennage aerodynamic interaction and helicopter trims. Proceedings of the Institution of Mechanical Engineers, Part G: Journal of Aerospace Engineering, Vol. 229, No. 3, pp 435–444, 2015. ISSN 0954-4100. doi: 10.1177/0954410014534203.

[8] Thiele M. Erweiterung und Validierung eines Rotortools mit Vorbereitung einer Konfigurationsstudie. Masterthesis, Technical University Munich- TUM, München, 2016. URL https://elib.dlr.de/106110/.

[9] Thiele M, Obster M and Hornung M. Aerodynamic modeling of coaxial counter-rotating uav propellers. In Vertical Flight Society , editor, 8th Biennial Autonomous VTOL Technical Meeting & 6th Annual Electric VTOL Symposium, 2019.

[10] Katz J and Plotkin A. Low-Speed Aerodynamics, Vol. 13 of Cambridge aerospace series. 2nd ed. edition, Cambridge University Press, 2001. ISBN 9780521662192.

[11] Preidikman S. Numerical Simulations of Interactions Among Aerodynamics, Structural Dynamics, and Control Systems. Dissertation, Virginia Polytechnic, Blacksburg, Virginia, 1998.

[12] Schlichting H and Truckenbrodt EA. Aerodynamik des Flugzeuges: Erster Band: Grundlagen aus der Strömungstechnik Aerodynamik des Tragflügels (Teil I), Vol. / H. Schlichting; E. Truckenbrodt ; Bd.1 of Klassiker der Technik. 3., aufl. 2001 [neuausg.] edition, Springer Berlin, 2013. ISBN 978-3-642-63148-1.

[13] Leishman JG. Principles of helicopter aerodynamics. Cambridge aerospace series. Second edition edition, Cambridge University Press, 2016. ISBN 1107013356.

[14] Bhagwat MJ and Leishman JG. Generalized viscous vortex model for application to free-vortex wake and aeroacoustic calculations. In Vertical Flight Society , editor, 58th Annual Forum and Technology Display of the American Helicopter Society International, 2002. ISBN 9781617829352. URL https://www.researchgate.net/publication/255470975_Generalized_viscous_vortex_model_for_application_to_free-vortex_wake_and_aeroacoustic_calculations.

[15] Vatistas GH, Kozel V and Mih WC. A simpler model for concentrated vortices. Experiments in Fluids, Vol. 11, No. 2, pp 73–76, 1991. ISSN 0723-4864. URL https://doi.org/10.1007/BF00198434.

[16] Bagai A and Leishman J. Flow visualization of compressible vortex structures using density gradient techniques. Experiments in Fluids, Vol. 15, No. 6, 1993. ISSN 0723-4864. doi: 10.1007/BF00191786.

[17] Lamb H. Hydrodynamics. 6 edition, Cambridge University Press, 1932.

[18] Griffiths DA, Ananthan S and Leishman JG. Predictions of rotor performance in ground effect using a free-vortex wake model. Journal of the American Helicopter Society, Vol. 50, No. 4, pp 302–314, 2005. doi: 10.4050/1.3092867.

[19] Johnson W. Rotorcraft aeromechanics, Vol. 36 of Cambridge aerospace series. Cambridge University Press, 2013. ISBN 978-1-107-02807-4. URL https://doi.org/10.1017/CBO9781139235655.

[20] Colmenares JD, López OD and Preidikman S. Computational study of a transverse rotor aircraft in hover using the unsteady vortex lattice method. Mathematical Problems in Engineering, Vol. 2015, No. 1, pp 1–9, 2015. ISSN 1024-123X. doi: 10.1155/2015/478457.

[21] Ost J. Parameterbasierte Modellierung von Rotor-Anstroemungszustaenden. Bachelorsthesis, Technical University of Munich, Garching, 2017.

[22] D'Errico J. Inhull, 2020. URL https://www.mathworks.com/matlabcentral/fileexchange/10226-inhull.

[23] Hazewinkel M. Encyclopaedia of mathematics. Springer-Verlag, 2002. ISBN 9781402006098.

[24] Kiefer J. Sequential minimax search for a maximum. Proceedings of the American Mathematical Society, Vol. 4, No. 3, pp 502, 1953. ISSN 0002-9939. doi: 10.1090/S0002-9939-1953-0055639-3.

[25] Perdolt D, Thiele M, Milz D, May M, Kuchar R and Hornung M. Comparison of mid-fidelity rotor analysis tools for transitional and low speed flight regimes. In Deutscher Luft- und Raumfahrtkongress 2021. Deutsche Gesellschaft für Luft- und Raumfahrt - Lilienthal-Oberth e.V, 2021.

[26] Caradonna FX and Tung C. Experimental and analytical studies of a model helicopter rotor in hover. URL https://ntrs.nasa.gov/search.jsp?R=19820004169.

[27] Kolaei A, Barcelos D and Bramesfeld G. Experimental analysis of a small-scale rotor at various inflow angles. International Journal of Aerospace Engineering, Vol. 2018, pp 1–14, 2018. ISSN 1687-5966. doi: 10.1155/2018/2560370.

[28] Brandt J and Selig M. Propeller performance data at low reynolds numbers. In 49th AIAA Aerospace Sciences Meeting including the New Horizons Forum and Aerospace Exposition, 2011. doi: 10.2514/6.2011-1255.

[29] Cai J, Gunasekaran S, Ahmed A and Ol MV. Changes in propeller performance due to ground proximity. In AIAA , editor, AIAA Scitech 2019 Forum, Reston, Virginia, 2019. American Institute of Aeronautics and Astronautics. ISBN 978-1-62410-578-4. doi: 10.2514/6.2019-1097.

[30] Cai J, Gunasekaran S, Ahmed A and Ol MV. Propeller partial ground effect. In AIAA , editor, AIAA Scitech 2020 Forum, page 24, Reston, Virginia, 2020. American Institute of Aeronautics and Astronautics. ISBN 978-1-62410-595-1. doi: 10.2514/6.2020-1028.